

Ultralow-power chip-based soliton microcombs for photonic integration

Junqiu Liu,^{1,*} Arslan S. Raja,^{1,*} Maxim Karpov,¹ Bahareh Ghadiani,¹ Martin H. P. Pfeiffer,¹ Nils J. Engelsen,¹ Hairun Guo,¹ Michael Zervas,² and Tobias J. Kippenberg^{1,†}

¹*École Polytechnique Fédérale de Lausanne (EPFL), CH-1015 Lausanne, Switzerland*

²*LIGENEC SA, CH-1015 Lausanne, Switzerland*

(Dated: October 5, 2018)

The generation of dissipative Kerr solitons in optical microresonators has provided a route to compact frequency combs of high repetition rate, which have already been employed for optical frequency synthesizers, ultrafast ranging, coherent telecommunication and dual-comb spectroscopy. Silicon nitride (Si_3N_4) microresonators are promising for photonic integrated soliton microcombs. Yet to date, soliton formation in Si_3N_4 microresonators at electronically detectable repetition rates, typically less than 100 GHz, is hindered by the requirement of external power amplifiers, due to the low quality (Q) factors, as well as by thermal effects which necessitate the use of frequency agile lasers to access the soliton state. These requirements complicate future photonic integration, heterogeneous or hybrid, of soliton microcomb devices based on Si_3N_4 microresonators with other active or passive components. Here, using the photonic Damascene reflow process, we demonstrate ultralow-power single soliton formation in high- Q ($Q_0 > 15 \times 10^6$) Si_3N_4 microresonators with 9.8 mW input power (6.2 mW in the waveguide) for devices of electronically detectable, 99 GHz repetition rate. We show that solitons can be accessed via simple, slow laser piezo tuning, in many resonances in the same sample. These power levels are compatible with current silicon-photonics-based lasers for full photonic integration of soliton microcombs, at repetition rates suitable for applications such as ultrafast ranging and coherent communication. Our results show the technological readiness of Si_3N_4 optical waveguides for future all-on-chip soliton microcomb devices.

I. INTRODUCTION

Optical frequency combs^{1,2} have revolutionized time-keeping and metrology over the past decades, and have found a wide variety of applications³. First discovered more than a decade ago, microresonator-based Kerr frequency combs ("microcomb")^{4,5} are providing a route to chip-scale optical frequency combs, with broad bandwidth and repetition rates in the GHz to THz domain. Such microcombs have been demonstrated in a wide variety of platforms, including CMOS compatible materials such as silicon nitride (Si_3N_4)^{6,7}, which al-

lows full photonic integration with other devices on silicon, active or passive, such as lasers⁸, modulators⁹ and photodetectors¹⁰. The demonstration of microcombs in the dissipative Kerr soliton (DKS) regime¹¹ has unlocked the full potential of microcombs, by allowing reliable access to fully coherent comb states, which can attain large bandwidth via soliton Cherenkov radiation¹²⁻¹⁴. Such soliton microcombs have already been successfully applied in counting the cycles of light¹⁵, coherent communication on the receiver and transmitter sides¹⁶, dual-comb spectroscopy¹⁷, ultrafast optical ranging^{18,19}, astrophysical spectrometer calibration^{20,21}, and for creating a photonic integrated frequency synthesizer²². These developments highlight the potential of chip-scale soliton microcombs for timing, metrology and spectroscopy, allowing unprecedentedly compact devices at low operation power, fully compatible with wafer-scale fabrication and suitable for operation in space²³.

A particularly promising platform for photonic integrated soliton microcombs is Si_3N_4 , a material that has a wide transparency window and high material optical nonlinearity. Recent advances in fabrication have enabled access to the anomalous group velocity dispersion regime (GVD) with sufficient waveguide height²⁴, and circumvented the problems associated with the high tensile stress of Si_3N_4 film²⁵. Although the soliton microcomb has been directly generated with a diode laser in a silica microresonator coupled to a tapered optical fiber recently²⁶, this has not been possible for integrated devices including Si_3N_4 . Yet, there are remaining challenges in soliton formation in Si_3N_4 microresonators, related to: (i) The comparatively low quality (Q) factor which increases the threshold power of soliton formation, compared to e.g. crystalline and silica microresonators. (ii) Optical coupling losses from the laser to the chip device, resulting from the optical mode mismatch at chip facets. (iii) Stable access to soliton states may require the use of complex excitation techniques such as "power kicking"²⁷ or single-sideband modulators²⁸. The first two challenges are particularly problematic for future photonic integration, as they necessitate the use of high-power lasers. So far, for integrated Si_3N_4 microresonator devices, soliton formation with device input power of several hundreds of milliwatts has only been achieved in microresonators of 1 THz free spectral range (FSR)^{22,29-31}. Yet in these experiments input coupling loss still necessitated the use of additional amplifiers to reach the required power levels of several tens of milliwatts on the chip. Meanwhile, low microcomb initi-

ation power at milliwatt or even sub-milliwatt level has been demonstrated in Si_3N_4 microresonators of Q exceeding 10^7 ^{32,33}, but solitons have not been observed due to the insufficient anomalous GVD. Consequently, soliton formation has been limited to wavelength regions where optical amplifiers are available. It is only very recently that soliton generation in high- Q Si_3N_4 microresonators of anomalous GVD pumped by an integrated laser was reported in Ref.³⁴. However in that case, the repetition rate is 200 GHz, which is not electronically detectable, resulting in limited application potentials.

Here we demonstrate that the newly developed variant of photonic Damascene process^{35,36}, the *photonic Damascene reflow* process³⁷, can overcome the outlined challenges and significantly reduce the required input power for soliton formation in Si_3N_4 microresonators. We demonstrate single soliton formation in Si_3N_4 microresonators of $Q_0 > 8.2 \times 10^6$ at the lowest repetition rate to date of 88 GHz, which is electronically detectable, with 48.6 mW power at the chip input facet (30.3 mW in the bus waveguide). In addition, by further improving the microresonator Q factors to $Q_0 > 15 \times 10^6$, we demonstrate single soliton formation of 99 GHz repetition rate with a record-low input power of 9.8 mW (6.2 mW in the waveguide). Using only a tunable diode laser without an optical amplifier, we access single soliton states in eleven consecutive resonances in the telecom L-band and five in the telecom C-band, via simple laser piezo tuning. Such low-power soliton microcombs of sub-100-GHz repetition rate can significantly simplify the recently demonstrated dual-comb ultrafast distance measurements¹⁸ and optical coherent communication¹⁶, which required Erbium-doped fiber amplifiers (EDFA) to amplify the input power to above 1 Watt. In addition, the soliton microcombs demonstrated here have shown great potential for future photonic integrated microwave generators, and chip-based frequency synthesizers²² via integration of on-chip lasers, semiconductor optical amplifiers and nonlinear microresonators. Soliton microcombs formed in wavelength regions where amplifiers are not available could unlock new applications such as optical coherent tomography (OCT) at $1.3 \mu\text{m}$ ³⁸ and sensing of toxic gases and greenhouse gases e.g. methane at $1.6 \mu\text{m}$ ³⁹.

II. SAMPLE FABRICATION

Here, we briefly describe our fabrication process of Si_3N_4 microresonator samples. The waveguide is patterned on photoresist on the silicon dioxide (SiO_2) substrate, using deep-UV (DUV) stepper lithography. The pattern is then transferred from the DUV photoresist to the SiO_2 substrate via reactive ion etching (RIE) using C_4F_8 , O_2 and helium. Before the Si_3N_4 deposition on the patterned substrate using low pressure chemical vapor deposition (LPCVD), we do a "preform reflow"³⁷, where the substrate is annealed at 1250°C temperature

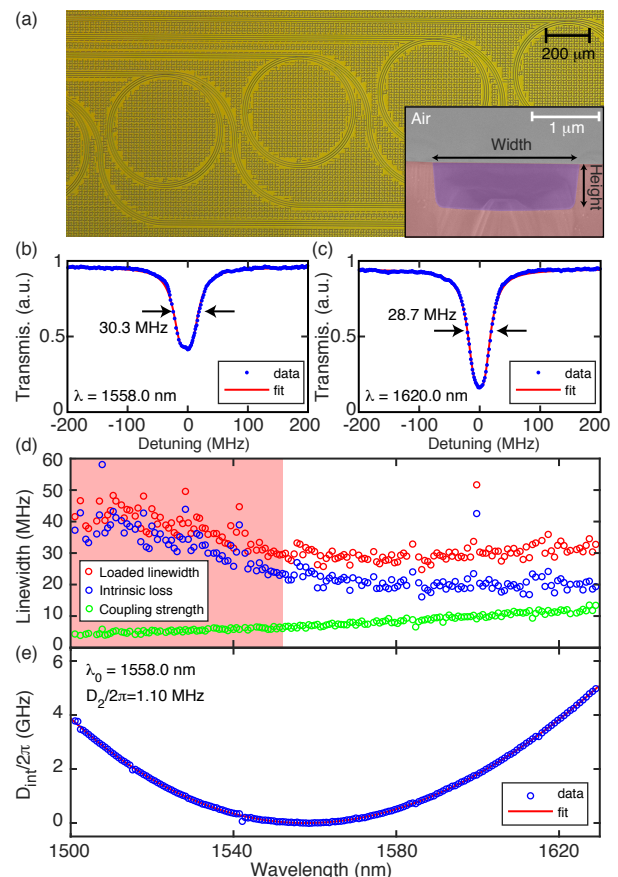


Figure 1. Dispersion and resonance linewidth characterization of a 88-GHz-FSR microresonator. (a) Microscope image of densely packed 88-GHz-FSR microresonators, using meander bus waveguides. These samples have no SiO_2 top cladding. Inset: SEM image of the cross-section of a Si_3N_4 waveguide without SiO_2 top cladding. The Si_3N_4 waveguide is blue shaded, the SiO_2 bottom cladding is red shaded, the air is not color shaded. (b) The pump resonance at $\lambda = 1558.0$ nm and its fit, with the loaded linewidth of $\kappa/2\pi = 30.3$ MHz and fitted intrinsic loss of $\kappa_0/2\pi \sim 23.2$ MHz, corresponding to $Q_0 > 8.2 \times 10^6$. (c) The resonance at $\lambda = 1620.0$ nm and its fit, with the loaded linewidth of $\kappa/2\pi = 28.7$ MHz and fitted intrinsic loss of $\kappa_0/2\pi \sim 17.3$ MHz, corresponding to $Q_0 > 10.7 \times 10^6$. (d) Loaded linewidth, intrinsic loss and coupling strength of each TE_{00} resonance. Larger intrinsic loss is found in the wavelength region from 1500 to 1550 nm (red shaded area), due to the absorption by the N-H and Si-H bonds in LPCVD Si_3N_4 . (e) Measured GVD of the TE_{00} mode family. Several avoided mode crossings are observed, where resonance linewidth increases.

with atmospheric pressure. Due to the high temperature and the SiO_2 surface tension, the sidewall roughness caused by the RIE on the SiO_2 preform is reduced, which reduces scattering losses and leads to ultra-smooth waveguide side surfaces. This helps to improve the Q of our Si_3N_4 microresonators.

The LPCVD Si_3N_4 film is deposited on the SiO_2 substrate, filling the preform trenches and defining the Si_3N_4

waveguides. The deposition is followed by chemical-mechanical polishing (CMP) which removes the excess Si_3N_4 and creates an ultrasmooth waveguide top surface. The substrate is annealed at 1200°C in nitrogen atmosphere, to drive out the residual hydrogen content introduced from the SiH_2Cl_2 and NH_3 utilized in the LPCVD Si_3N_4 process. Adding SiO_2 top cladding is optional, while both situations are considered in our work, which will be described later. Finally, the wafer is separated into chips by dicing or with deep RIE. More details of fabrication process are found in Ref.³⁶ and³⁷.

For integrated chip-based nonlinear photonics, inverse nanotapers⁴⁰ are widely used as chip input couplers and can achieve high fiber-chip-fiber coupling efficiency and broad operation bandwidth. The standard subtractive process^{32,41} requires the taper width to be less than 100 nm, to achieve fiber-chip-fiber coupling efficiency of 40% or more. Thus the resolution of DUV stepper lithography is incompatible with the subtractive process, which requires instead electron beam lithography. For the Damascene process, the required optimum taper width is above 400 nm, to attain 40% coupling efficiency, thus the DUV stepper lithography is compatible with this process. The high coupling efficiency with much larger taper width, compared with the one used in the subtractive process, is due the strong aspect-ratio-dependent etch rate⁴² of the preform RIE, which is specifically engineered to allow the creation of *double-inverse nanotapers* as chip input couplers (more details are found in Ref.⁴³). The double-inverse nanotaper enables high coupling efficiency (40% or more) with large taper width (above 400 nm) for both the transverse-electric (TE) and transverse-magnetic (TM) polarizations, due to the reduced taper height, which increases the evanescent field size at the taper tip, thus improving the mode match between the taper mode to the incident lensed fiber mode⁴³.

III. SOLITON COMB OF 88 GHz REPETITION RATE

In the first part, we demonstrate single soliton formation in 88-GHz-FSR microresonators, with the fundamental TE mode (TE_{00}). Fig. 1(a) shows the microscope image of the 88-GHz-FSR microresonators. The microresonator samples described in this section have no SiO_2 top cladding, as shown in Fig. 1(a) inset. Meander bus waveguides are used to densely pack a large number of devices on one chip. The Si_3N_4 microresonator has a cross-section, width \times height, of $1.58 \times 0.75 \mu\text{m}^2$, and is coupled to a multi-mode bus waveguide of the same cross-section for high coupling ideality⁴⁴. The polarization of the incident light to the chip is controlled by fiber polarization controllers, and the polarization state is measured using linear polarizers. The microresonator transmission trace is obtained from 1500 to 1630 nm using frequency-comb-assisted diode laser spectroscopy^{45,46}. The precise frequency of each data point is calibrated using a com-

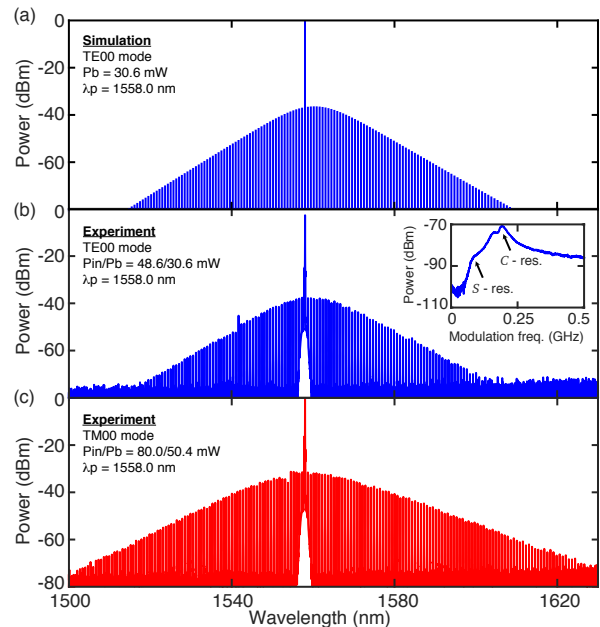


Figure 2. Single soliton formation in the 88-GHz-FSR microresonator. (a) Simulated single soliton spectrum based on the measured microresonator's parameters, in the TE_{00} mode. $P_b = 30.6$ mW corresponds to $P_{in} = 48.6$ mW. (b) Single soliton spectrum pumped at $\lambda_p = 1558.0$ nm in the TE_{00} mode, with a pump power of $P_{in} = 48.6$ mW ($P_b = 30.6$ mW). Inset: cavity response measurement using the VNA, verifying that the spectrum is a single soliton state. (c) Single soliton spectrum pumped at $\lambda_p = 1558.0$ nm in the TM_{00} mode, with the pump power $P_{in} = 80.0$ mW ($P_b = 50.4$ mW).

mercial femtosecond optical frequency comb with 250 MHz repetition rate. For the TE_{00} mode family, the FSR of the microresonator and the anomalous GVD are extracted from the calibrated transmission trace by identifying the precise frequency of each resonance. The total (loaded) linewidth $\kappa/2\pi = (\kappa_0 + \kappa_{ex})/2\pi$, the intrinsic linewidth (intrinsic loss) $\kappa_0/2\pi$ and the coupling strength $\kappa_{ex}/2\pi$ are extracted from each resonance fit^{47,48}.

The measured linewidths of each TE_{00} resonance are shown in Fig. 1(d). These resonances are all under-coupled. Larger linewidths are found in the wavelength region from 1500 to 1550 nm, due the absorption by the nitrogen-hydrogen (N-H) and silicon-hydrogen (Si-H) bonds in LPCVD Si_3N_4 material^{49,50}. These bonds are introduced during standard LPCVD Si_3N_4 process based on SiH_2Cl_2 and NH_3 precursors⁵¹, and can be partially removed by thermal annealing. Fig. 1(b) shows the resonance at $\lambda = 1558.0$ nm. The resonance fit shows a loaded linewidth of $\kappa/2\pi = 30.3$ MHz, and the estimated intrinsic loss based on the resonance fit is $\kappa_0/2\pi \sim 23.3$ MHz, corresponding to the intrinsic $Q_0 > 8.2 \times 10^6$. Fig. 1(c) shows the resonance at $\lambda = 1620.0$ nm, with a loaded linewidth of $\kappa/2\pi = 28.7$ MHz, and the estimated intrinsic loss is $\kappa_0/2\pi \sim 17.3$ MHz, corresponding to the intrinsic $Q_0 > 10.7 \times 10^6$. Fig. 1(e) shows

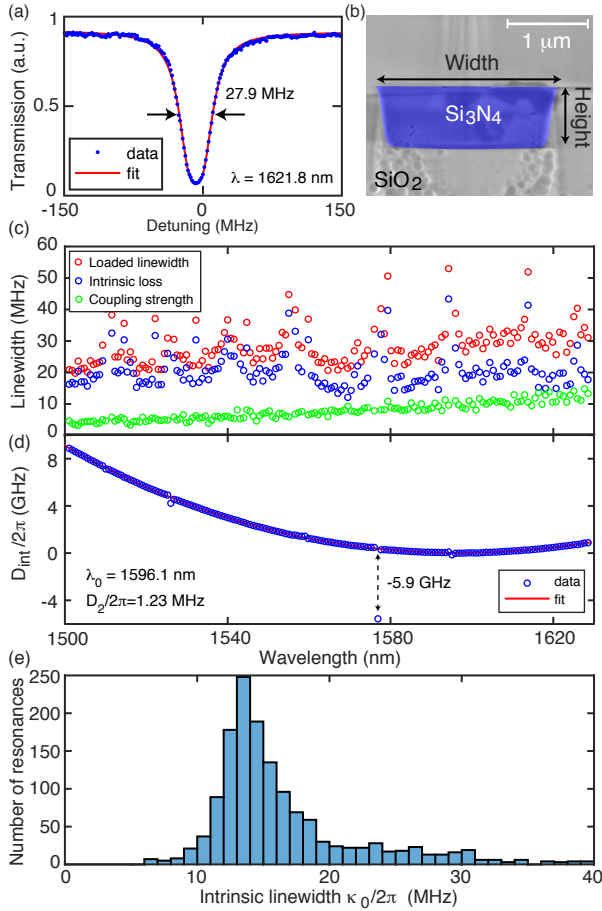


Figure 3. Dispersion and resonance linewidth characterization of a 99-GHz-FSR microresonator. (a) The critically coupled resonance at $\lambda = 1621.8$ nm and its fit, with the loaded linewidth of $\kappa_0/2\pi = 27.9$ MHz and fitted intrinsic loss of $\kappa_0/2\pi \sim 13.7$ MHz. (b) SEM image of the cross-section of a Si_3N_4 waveguide with full SiO_2 cladding. The Si_3N_4 waveguide is blue shaded, the SiO_2 cladding is not color shaded. (c) Loaded linewidth, intrinsic loss and coupling strength of each TE_{00} resonance. No prominent hydrogen absorption loss is observed in the wavelength region from 1500 to 1550 nm. (d) Measured GVD of the TE_{00} mode family. Several avoided mode crossings are observed, where resonance linewidth increases. A strong mode crossing is found at 1577 nm, with -5.9 GHz resonance frequency deviation. (e) Histogram of intrinsic loss from the measurement of eight under-coupled samples. The most probable value of the histogram is around 13 - 14 MHz, which represents the Q factor of $Q_0 > 15 \times 10^6$.

the measured microresonator integrated GVD, defined as $D_{\text{int}}(\mu) = \omega_\mu - \omega_0 - D_1\mu = D_2\mu^2/2 + D_3\mu^3/6 + \dots$ ⁴⁶. Here $\omega_\mu/2\pi$ is the frequency of the μ -th resonance relative to the reference resonance $\omega_0/2\pi = 192.6$ THz ($\lambda_0 = 1558.0$ nm, as shown in Fig.1(b)). $D_1/2\pi$ corresponds to the FSR. D_2 , D_3 and other higher order terms determine the GVD profile. The fit values obtained from the dispersion measurement are $D_1/2\pi \sim 88.63$ GHz, $D_2/2\pi \sim 1.10$ MHz and $D_3/2\pi \sim \mathcal{O}(1)$ kHz.

When the pump laser scans over the resonance from

the blue-detuned side to the red-detuned side, a step in the transmission trace can be observed, signaling to the soliton formation¹¹. To generate and characterize soliton states, we use a setup as describe in Ref.⁵². Fiber-chip-fiber transmission of 40% (coupling efficiency of 63% per device facet) is achieved via double-inverse nanotapers on the chip facets⁴³. The input power (P_{in}) is defined as the power measured before the input lensed fiber which couples light into the chip device. Thus the optical power in the bus waveguide (P_{b}) on the chip, which directly pumps the microresonator, is calculated as $P_{\text{b}} = 0.63P_{\text{in}}$.

In our setup, the output power of the diode laser can go as high as 23 mW, with few milliwatt power variation depending on the wavelength. We use an EDFA to slightly amplify the optical power to $P_{\text{in}} = 48.6$ mW ($P_{\text{b}} = 30.6$ mW). To access the single soliton state, we use a single-sideband modulator²⁸, and a single soliton spectrum is observed as shown in Fig. 2(b), verified by the system response measurement using vector network analyzer (VNA)⁵². The observed double resonance response shown in Fig. 2(b) inset corresponds to the cavity resonance of the continuous wave ("C-resonance"), and the soliton-induced resonance ("S-resonance"). These two resonances can be distinguished by increasing the detuning of the soliton state⁵². Fig. 2(a) shows the simulation of soliton formation based on Lugiato-Lefever equation^{53,54} using the measured microresonator parameters. The simulated soliton spectrum is nearly identical to the measured one. We also generate a single soliton in the TM_{00} mode ($D_1/2\pi \sim 86.35$ GHz, $D_2/2\pi \sim 0.967$ MHz, $D_3/2\pi \sim 5.4$ kHz) pumped at the wavelength $\lambda_{\text{p}} = 1558.0$ nm, with the input power $P_{\text{in}} = 80.0$ mW ($P_{\text{b}} = 50.6$ mW), as shown in Fig. 2(c). This soliton spectrum is broader than the one in the TE_{00} mode shown in Fig. 2(b), likely due to the lower D_2 value and higher power. The estimated power conversion efficiency from the CW pump to the soliton pulse is around 1.5%, with the power per comb line around 20 μW in the 3 dB bandwidth. Compared to prior works shown in Ref.^{16,18} which use solitons of repetition rate less than 100 GHz with input power exceeding 1 Watt, our work represents a significant power reduction, while the power per comb line of 20 μW still can achieve the same goals as Ref.^{16,18}.

IV. SOLITON COMB OF 99 GHz REPETITION RATE

In the second part of our work, we demonstrate single soliton formation in 99-GHz-FSR microresonators. Fig. 1(d) shows that hydrogen absorption is the main loss reason which prevents the generation of 88 GHz soliton with lower power. Therefore we further improved the fabrication process, in order to remove hydrogen absorption losses. Note that, the hydrogen is likely introduced due to the incomplete thermal annealing, or moisture in the air which forms a thin water film on the sample surface, or a combination of both two. Therefore in

a new wafer fabrication run, we annealed the LPCVD Si_3N_4 via deposition - annealing - deposition - annealing cycles, as described in Ref.⁵⁵. To prevent water film formation on the wafer, a thick SiO_2 top cladding composed of TEOS and low temperature oxide (LTO) was deposited via LPCVD on the Si_3N_4 waveguides (SEM image of the waveguide cross-section is shown in Fig. 3(b)), followed by thermal annealing. Simultaneously, the dry etching process which patterns the SiO_2 preform was optimized, to further reduce mask damage and sidewall passivation, which can reduce the waveguide sidewall roughness and the number of defects. Fig. 3(c) shows the loaded linewidth, intrinsic loss and coupling strength of each TE_{00} resonance of a Si_3N_4 microresonator whose cross-section, width \times height, is $1.58 \times 0.81 \mu\text{m}^2$. The microresonator FSR is $D_1/2\pi \sim 98.9$ GHz. Compared with Fig. 1(d), Fig. 3(c) shows significant reduction of intrinsic loss in the wavelength range from 1500 to 1550 nm, demonstrating the successful removal of hydrogen in LPCVD Si_3N_4 . Some resonances with large linewidth are caused by avoided mode crossings, in accordance with the observed avoided mode crossings in the dispersion measurement shown in Fig. 3(d). The measured GVD is $D_2/2\pi \sim 1.23$ MHz, with respect to $\omega_0/2\pi = 188.0$ THz ($\lambda_0 = 1596.1$ nm as the pump resonance in Fig. 4). Figure 3(e) shows the histogram of intrinsic loss from the measurement of eight under-coupled samples. These samples have the same waveguide cross-section but different bus-waveguide-to-microresonator gap distance. The most probable value of the histogram is around 13 - 14 MHz, which represents the Q factor of $Q_0 > 15 \times 10^6$. Fig. 3(a) shows the resonance at $\lambda = 1621.8$ nm and its fit, with the loaded linewidth of $\kappa/2\pi = 27.9$ MHz and fitted intrinsic loss of $\kappa_0/2\pi \sim 13.7$ MHz.

Silicon nitride microresonators of anomalous GVD and Q factor exceeding 10×10^6 have been reported^{32,33}, however single soliton generation has not been demonstrated. In those works, large waveguide width ($\geq 2.5 \mu\text{m}$) was used. Despite the fact that the large waveguide width reduces optical mode interaction with the waveguide sidewall roughness, and thus reduces the scattering loss caused by the sidewall roughness, the resulted weak anomalous GVD due to the large waveguide width is insufficient for single soliton generation with low power. Here, with the high Q and strong anomalous GVD ($D_2/2\pi \sim 1.23$ MHz), we generate a single soliton of 99 GHz repetition rate with 9.8 mW input power (6.2 mW power in the bus waveguide), directly from the diode laser, without EDFA. The experimental setup is shown in Fig. 4(a), and the single soliton spectra are shown in Fig. 4(b). Parametric oscillation which generates frequency sidebands is observed around 1.7 mW chip input power. When the diode laser scans over the resonance, the observed soliton step varies from several hundred of microsecond to a millisecond (a representative soliton step in the transmission trace is shown in Fig. 4(c)), which is sufficiently long for accessing the single soliton state via simple laser piezo tuning¹¹. Increasing

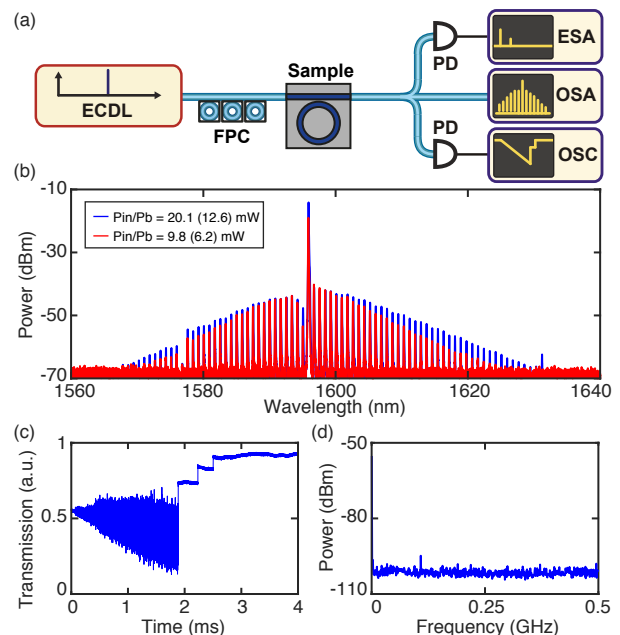


Figure 4. Single soliton formation in a 99-GHz-FSR microresonator without EDFA. (a) Experimental setup. EC DL: external-cavity diode laser. OSC: oscilloscope. OSA: optical spectrum analyzer. ESA: electrical spectrum analyzer. FPC: fiber polarization controller. PD: photodiode. (b) Single soliton spectra pumped at $\lambda_p = 1596.1$ nm in the TE_{00} mode, with the input pump powers of $P_{\text{in}} = 9.8$ mW ($P_b = 6.2$ mW, red) and $P_{\text{in}} = 20.1$ mW ($P_b = 12.6$ mW, blue). (c) A representative soliton step of several hundred of microsecond, sufficiently long for accessing the single soliton state via simple laser piezo tuning. (d) Low-frequency RF spectrum of the optical spectrum with $P_{\text{in}} = 9.8$ mW (red), demonstrating the soliton nature of the spectrum.

power to the maximum laser output (around 20.1 mW) increases the soliton bandwidth. The estimated power conversion efficiency from the CW pump to the soliton pulse is around 1.7%. To identify the soliton nature of the spectrum, in this case a VNA measurement is difficult to implement due to the large EOM insertion loss and the limited diode laser output power. Instead, the soliton nature is revealed by the low-frequency radio frequency (RF) spectrum, as shown in Fig. 4(d), which can be well distinguished from the recorded noisy comb spectrum (modulation instability, not shown here). We observed that, the single soliton generation with less than 10 mW input power is highly reproducible in resonances close to avoided mode crossings. In our case, without the EDFA and its gain bandwidth limitation, we tune the diode laser frequency to a resonance which is close to a mode crossing, and investigate the minimum power for single soliton generation. We have experimentally measured several samples, and observed that such sub-10-mW-power single soliton generation is highly reproducible in these resonances, all of which feature long soliton steps (similar to the one shown in Fig. 4(c)). It

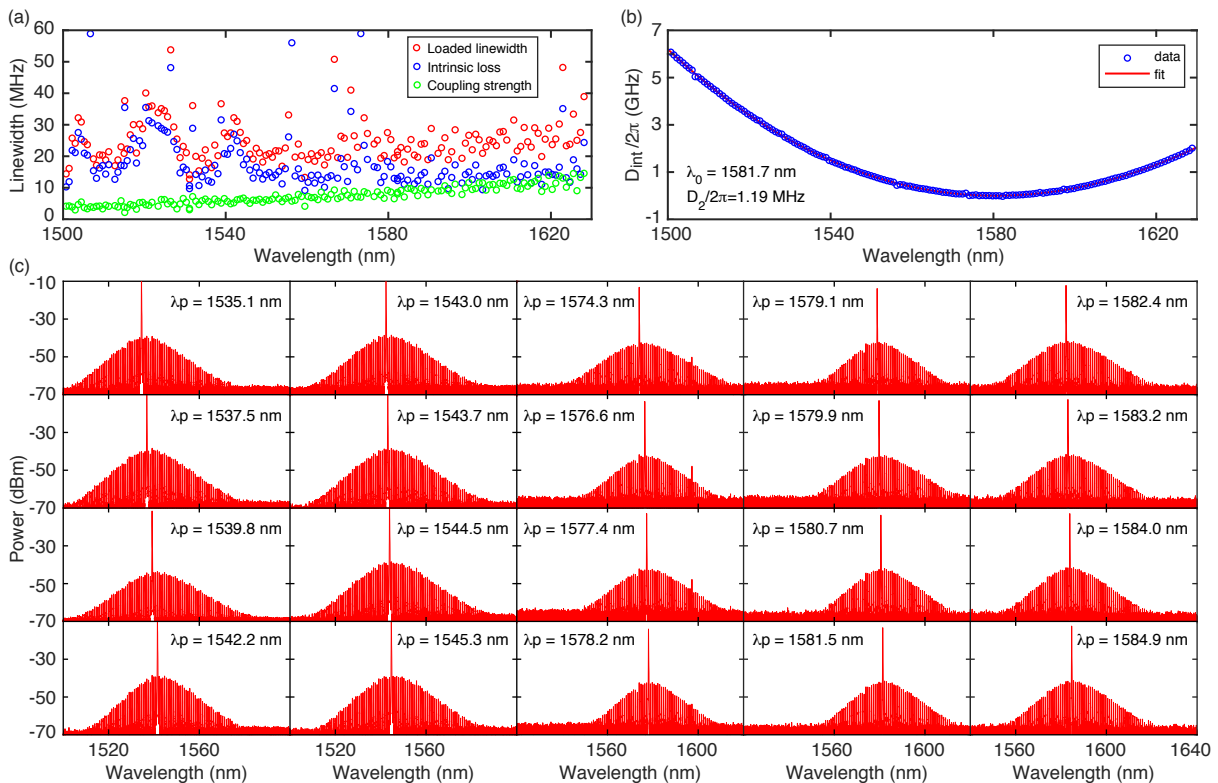


Figure 5. Characterization of a different 99-GHz-FSR microresonator, and single soliton formation in multiple resonances. (a) Loaded linewidth, intrinsic loss and coupling strength of each TE_{00} resonance. (b) Measured GVD of the TE_{00} mode family. (c) Single soliton formation in twenty selected resonances, eleven of which are consecutive in the telecom L-band, and five of which are consecutive in the telecom C-band. λ_p is the wavelength of the pumped resonance. The complete hydrogen removal facilitates the soliton generation in the hydrogen absorption band.

appears that the mode crossings can facilitate single soliton formation with lower power, compared with normal resonances far from mode crossings. This phenomenon is likely due to single soliton generation assisted by spatial mode-interactions⁵⁶.

We further investigate the single soliton formation over the full tuning range of the diode laser. Fig. 5(a), (b) show the measured resonance linewidth and microresonator dispersion of a different 99-GHz-FSR microresonator ($D_1/2\pi \sim 98.9$ GHz, $D_2/2\pi \sim 1.19$ MHz, $D_3/2\pi \sim -1.1$ kHz). Fig. 5(c) shows the single soliton spectra pumped at twenty selected resonances, eleven of which are consecutive in the telecom L-band, and five of which are consecutive in the telecom C-band. These spectra are generated with laser output power around 22 mW, and all accessed via simple laser piezo tuning. The complete hydrogen removal facilitates the soliton generation in the hydrogen absorption band. We did not investigate the minimum power to generate soliton in these resonances. We have also accessed single or few soliton state in other resonances in the same sample, in addition to the ones shown in Fig. 5(c). The single soliton generation in a broad range of resonances demonstrates the reliability of our fabrication process, and offers extra flexibility to investigate spectrally localized effects, such

as avoided mode crossings, which can enable the formation of dark pulses in the normal GVD region^{57,58}, and breathing solitons⁵⁹.

V. CONCLUSION

In summary, we present ultralow-power single soliton formation in integrated high- Q Si_3N_4 microresonators of sub-100-GHz FSR. We demonstrate soliton formation in a 88-GHz-FSR microresonator at 48.6 mW input power. The ultralow-power soliton formation results mainly from the microresonator's high Q (estimated intrinsic $Q_0 > 8.2 \times 10^6$) and the $>40\%$ device-through coupling efficiency. In addition, by further improving the microresonator Q factor to $Q_0 > 15 \times 10^6$ and reducing the thermal effects due to hydrogen absorption, we demonstrate single soliton formation of 99 GHz repetition rate with a record-low input power of 9.8 mW (6.2 mW in the waveguide), accessed via simple laser piezo tuning. We demonstrate the simplicity of soliton tuning and result reproducibility in twenty selected resonances in the same sample. Our work demonstrates soliton microcomb generation in Si_3N_4 integrated microresonators with milliwatts power level, central for applications which

require low power consumption, such as photonic chip-based microwave generators, integrated frequency synthesizers, OCT and dual-comb spectroscopy.

Data availability: The code and data used to produce the plots within this Article are available on Zenodo⁶⁰. All other data used in this study are available from the corresponding authors upon reasonable request.

FUNDING INFORMATION

This work was supported by Contract HR0011-15-C-0055 (DODOS) from the Defense Advanced Research Projects Agency (DARPA), Defense Sciences Office (DSO), and by Swiss National Science Foundation un-

der grant agreement No. 161573 (precoR).

ACKNOWLEDGMENTS

The Si₃N₄ microresonator samples were fabricated in the EPFL center of MicroNanoTechnology (CMi). M.K. acknowledges the support from the European Space Technology Centre with ESA Contract No. 4000116145/16/NL/MH/GM and 4000118777/16/NL/GM respectively. H.G. acknowledges the support from the European Union's Horizon 2020 research and innovation program under Marie Skłodowska-Curie IF grant agreement No. 709249. We acknowledge Tiago Morais for the assistance in sample fabrication.

* J.L. and A.S.R. contributed equally to this work

† tobias.kippenberg@epfl.ch

- ¹ T. Udem, R. Holzwarth, and T. W. Hänsch, *Nature* **416**, 233 (2002).
- ² S. T. Cundiff and J. Ye, *Rev. Mod. Phys.* **75**, 325 (2003).
- ³ N. R. Newbury, *Nature Photonics* **5**, 186 (2011).
- ⁴ P. Del'Haye, A. Schliesser, O. Arcizet, T. Wilken, R. Holzwarth, and T. J. Kippenberg, *Nature* **450**, 1214 (2007).
- ⁵ T. J. Kippenberg, R. Holzwarth, and S. A. Diddams, *Science* **332**, 555 (2011).
- ⁶ J. S. Levy, A. Gondarenko, M. A. Foster, A. C. Turner-Foster, A. L. Gaeta, and M. Lipson, *Nature Photonics* **4**, 37 (2010).
- ⁷ D. J. Moss, R. Morandotti, A. L. Gaeta, and M. Lipson, *Nature Photonics* **7**, 597 (2013).
- ⁸ D. Liang and J. E. Bowers, *Nature Photonics* **4**, 511 EP (2010).
- ⁹ G. T. Reed, G. Mashanovich, F. Y. Gardes, and D. J. Thomson, *Nature Photonics* **4**, 518 EP (2010).
- ¹⁰ J. Michel, J. Liu, and L. C. Kimerling, *Nature Photonics* **4**, 527 EP (2010).
- ¹¹ T. Herr, V. Brasch, J. D. Jost, C. Y. Wang, N. M. Kondratiev, M. L. Gorodetsky, and T. J. Kippenberg, *Nature Photonics* **8**, 145 (2014).
- ¹² J. K. Jang, M. Erkintalo, S. G. Murdoch, and S. Coen, *Opt. Lett.* **39**, 5503 (2014).
- ¹³ C. Milián and D. Skryabin, *Opt. Express* **22**, 3732 (2014).
- ¹⁴ V. Brasch, M. Geiselmann, T. Herr, G. Lihachev, M. H. P. Pfeiffer, M. L. Gorodetsky, and T. J. Kippenberg, *Science* **351**, 357 (2016).
- ¹⁵ J. D. Jost, T. Herr, C. Lecaplain, V. Brasch, M. H. P. Pfeiffer, and T. J. Kippenberg, *Optica* **2**, 706 (2015).
- ¹⁶ P. Marin-Palomo, J. N. Kemal, M. Karpov, A. Kordts, J. Pfeifle, M. H. P. Pfeiffer, P. Trocha, S. Wolf, V. Brasch, M. H. Anderson, R. Rosenberger, K. Vijayan, W. Freude, T. J. Kippenberg, and C. Koos, *Nature* **546**, 274 (2017).
- ¹⁷ M.-G. Suh, Q.-F. Yang, K. Y. Yang, X. Yi, and K. J. Vahala, *Science* **354**, 600 (2016).
- ¹⁸ P. Trocha, M. Karpov, D. Ganin, M. H. P. Pfeiffer, A. Kordts, S. Wolf, J. Krockenberger, P. Marin-Palomo, C. Weimann, S. Randel, W. Freude, T. J. Kippenberg,

and C. Koos, *Science* **359**, 887 (2018).

- ¹⁹ M.-G. Suh and K. J. Vahala, *Science* **359**, 884 (2018).
- ²⁰ E. Obrzud, M. Rainer, A. Harutyunyan, M. Anderson, M. Geiselmann, B. Chazelas, S. Kundermann, S. Lecomte, M. Cecconi, A. Ghedina, E. Molinari, F. Pepe, F. Wildi, F. Bouchy, T. Kippenberg, and T. Herr, *arXiv* **1712.09526** (2017).
- ²¹ M.-G. Suh, X. Yi, Y.-H. Lai, S. Leifer, I. S. Grudinin, G. Vasisht, E. C. Martin, M. P. Fitzgerald, G. Doppmann, J. Wang, D. Mawet, S. B. Papp, S. A. Diddams, C. Beichman, and K. Vahala, *arXiv* **1801.05174v1** (2017).
- ²² D. T. Spencer, T. Drake, T. C. Briles, J. Stone, L. C. Sinclair, C. Fredrick, Q. Li, D. Westly, B. R. Ilic, A. Bluestone, N. Volet, T. Komljenovic, L. Chang, S. H. Lee, D. Y. Oh, M.-G. Suh, K. Y. Yang, M. H. P. Pfeiffer, T. J. Kippenberg, E. Norberg, L. Theogarajan, K. Vahala, N. R. Newbury, K. Srinivasan, J. E. Bowers, S. A. Diddams, and S. B. Papp, *Nature* (2018), 10.1038/s41586-018-0065-7.
- ²³ V. Brasch, Q.-F. Chen, S. Schiller, and T. J. Kippenberg, *Opt. Express* **22**, 30786 (2014).
- ²⁴ M. A. Foster, A. C. Turner, J. E. Sharping, B. S. Schmidt, M. Lipson, and A. L. Gaeta, *Nature* **441**, 960 (2006).
- ²⁵ K. Luke, A. Dutt, C. B. Poitras, and M. Lipson, *Opt. Express* **21**, 22829 (2013).
- ²⁶ N. Volet, X. Yi, Q. Yang, E. J. Stanton, P. A. Morton, K. Y. Yang, K. J. Vahala, and J. E. Bowers, *Laser Photonics Rev.* **0**, 1700307.
- ²⁷ V. Brasch, M. Geiselmann, M. H. P. Pfeiffer, and T. J. Kippenberg, *Opt. Express* **24**, 29312 (2016).
- ²⁸ J. R. Stone, T. C. Briles, T. E. Drake, D. T. Spencer, D. R. Carlson, S. A. Diddams, and S. B. Papp, *Phys. Rev. Lett.* **121**, 063902 (2018).
- ²⁹ Q. Li, T. C. Briles, D. A. Westly, T. E. Drake, J. R. Stone, B. R. Ilic, S. A. Diddams, S. B. Papp, and K. Srinivasan, *Optica* **4**, 193 (2017).
- ³⁰ M. H. P. Pfeiffer, C. Herkommer, J. Liu, H. Guo, M. Karpov, E. Lucas, M. Zervas, and T. J. Kippenberg, *Optica* **4**, 684 (2017).
- ³¹ T. C. Briles, J. R. Stone, T. E. Drake, D. T. Spencer, C. Fredrick, Q. Li, D. Westly, B. R. Ilic, K. Srinivasan, S. A. Diddams, and S. B. Papp, *Opt. Lett.* **43**, 2933 (2018).

- ³² Y. Xuan, Y. Liu, L. T. Varghese, A. J. Metcalf, X. Xue, P.-H. Wang, K. Han, J. A. Jaramillo-Villegas, A. A. Noman, C. Wang, S. Kim, M. Teng, Y. J. Lee, B. Niu, L. Fan, J. Wang, D. E. Leaird, A. M. Weiner, and M. Qi, *Optica* **3**, 1171 (2016).
- ³³ X. Ji, F. A. S. Barbosa, S. P. Roberts, A. Dutt, J. Cardenas, Y. Okawachi, A. Bryant, A. L. Gaeta, and M. Lipson, *Optica* **4**, 619 (2017).
- ³⁴ B. Stern, X. Ji, Y. Okawachi, A. L. Gaeta, and M. Lipson, *arXiv* **1804.00357** (2018).
- ³⁵ M. H. P. Pfeiffer, A. Kordts, V. Brasch, M. Zervas, M. Geiselmann, J. D. Jost, and T. J. Kippenberg, *Optica* **3**, 20 (2016).
- ³⁶ M. H. P. Pfeiffer, C. Herkommer, J. Liu, T. Morais, M. Zervas, M. Geiselmann, and T. J. Kippenberg, *IEEE Journal of Selected Topics in Quantum Electronics*, *IEEE Journal of Selected Topics in Quantum Electronics* **24**, 1 (2018).
- ³⁷ M. H. P. Pfeiffer, J. Liu, A. S. Raja, T. Morais, B. Ghadani, and T. J. Kippenberg, *Optica* **5**, 884 (2018).
- ³⁸ S. H. Yun, G. J. Tearney, B. E. Bouma, B. H. Park, and J. F. de Boer, *Opt. Express* **11**, 3598 (2003).
- ³⁹ L. Tombez, E. J. Zhang, J. S. Orcutt, S. Kamlapurkar, and W. M. J. Green, *Optica* **4**, 1322 (2017).
- ⁴⁰ V. R. Almeida, R. R. Panepucci, and M. Lipson, *Opt. Lett.* **28**, 1302 (2003).
- ⁴¹ A. Gondarenko, J. S. Levy, and M. Lipson, *Opt. Express* **17**, 11366 (2009).
- ⁴² R. A. Gottscho, C. W. Jurgensen, and D. J. Vitkavage, *J. Vac. Sci. Technol. B* **10**, 2133 (1992).
- ⁴³ J. Liu, A. S. Raja, M. H. P. Pfeiffer, C. Herkommer, H. Guo, M. Zervas, M. Geiselmann, and T. J. Kippenberg, *Opt. Lett.* **43**, 3200 (2018).
- ⁴⁴ M. H. P. Pfeiffer, J. Liu, M. Geiselmann, and T. J. Kippenberg, *Phys. Rev. Applied* **7**, 024026 (2017).
- ⁴⁵ P. Del’Haye, O. Arcizet, M. L. Gorodetsky, R. Holzwarth, and T. J. Kippenberg, *Nature Photonics* **3**, 529 (2009).
- ⁴⁶ J. Liu, V. Brasch, M. H. P. Pfeiffer, A. Kordts, A. N. Kamel, H. Guo, M. Geiselmann, and T. J. Kippenberg, *Opt. Lett.* **41**, 3134 (2016).
- ⁴⁷ M. L. Gorodetsky, A. D. Pryamikov, and V. S. Ilchenko, *J. Opt. Soc. Am. B* **17**, 1051 (2000).
- ⁴⁸ Q. Li, A. A. Eftekhar, Z. Xia, and A. Adibi, *Phys. Rev. A* **88**, 033816 (2013).
- ⁴⁹ S. C. Mao, S. H. Tao, Y. L. Xu, X. W. Sun, M. B. Yu, G. Q. Lo, and D. L. Kwong, *Opt. Express* **16**, 20809 (2008).
- ⁵⁰ J. F. Bauters, M. J. R. Heck, D. D. John, J. S. Barton, C. M. Bruinink, A. Leinse, R. G. Heideman, D. J. Blumenthal, and J. E. Bowers, *Opt. Express* **19**, 24090 (2011).
- ⁵¹ J. Yota, J. Hander, and A. A. Saleh, *J. Vac. Sci. Technol. A* **18**, 372 (2000).
- ⁵² H. Guo, M. Karpov, E. Lucas, A. Kordts, M. H. P. Pfeiffer, V. Brasch, G. Lihachev, V. E. Lobanov, M. L. Gorodetsky, and T. J. Kippenberg, *Nature Physics* **13**, 94 (2016).
- ⁵³ L. A. Lugiato and R. Lefever, *Phys. Rev. Lett.* **58**, 2209 (1987).
- ⁵⁴ S. Coen, H. G. Randle, T. Sylvestre, and M. Erkintalo, *Opt. Lett.* **38**, 37 (2013).
- ⁵⁵ K. Luke, Y. Okawachi, M. R. E. Lamont, A. L. Gaeta, and M. Lipson, *Opt. Lett.* **40**, 4823 (2015).
- ⁵⁶ C. Bao, Y. Xuan, D. E. Leaird, S. Wabnitz, M. Qi, and A. M. Weiner, *Optica* **4**, 1011 (2017).
- ⁵⁷ Y. Liu, Y. Xuan, X. Xue, P.-H. Wang, S. Chen, A. J. Metcalf, J. Wang, D. E. Leaird, M. Qi, and A. M. Weiner, *Optica* **1**, 137 (2014).
- ⁵⁸ X. Xue, Y. Xuan, Y. Liu, P.-H. Wang, S. Chen, J. Wang, D. E. Leaird, M. Qi, and A. M. Weiner, *Nature Photonics* **9**, 594 (2015).
- ⁵⁹ H. Guo, E. Lucas, M. H. P. Pfeiffer, M. Karpov, M. Anderson, J. Liu, M. Geiselmann, J. D. Jost, and T. J. Kippenberg, *Phys. Rev. X* **7**, 041055 (2017).
- ⁶⁰ <https://doi.org/10.5281/zenodo.1412765>.